MAXIMIZING CORNER EFFICIENCY FOR A LOW-SPEED CLOSED-RETURN WIND TUNNEL

By

Daniel J. Eager

A thesis submitted in partial fulfillment of the requirements for the degree of

Bachelor of Science

Houghton College

July 2018

Signature of Author……  ……

Department of Physics
July 25, 2018

……

Dr. Kurt Aikens
Assistant Professor of Physics
Research Supervisor

……

Dr. Mark Yuly
Professor of Physics

MAXIMIZING CORNER EFFICIENCY FOR A LOW-SPEED CLOSED-RETURN WIND TUNNEL

By

Daniel J. Eager

Submitted to the Department of Physics
on July 25, 2018 in partial fulfillment of the
requirement for the degree of
Bachelor of Science

Abstract

A low-speed closed-return wind tunnel is being designed and built at Houghton College. To aid in the design of the wind tunnel, empirical correlations were used to predict stagnation pressure losses in different sections of the wind tunnel based on design choices that were made. This was used to roughly size the wind tunnel, but some components need more detailed design – the corners are an example of this. In corners, turning vanes are commonly used to help minimize the stagnation pressure loss that is associated with changing the direction of the flow. To determine the optimal number of vanes, simulations were conducted using ANSYS Fluent. Vanes with an airfoil cross-section were utilized since they are more efficient than single-walled vanes, are better equipped to handle fluid flows at different incoming angles, and are commercially available. The numerical results will be presented and future work discussed.

Thesis Supervisor: Dr. Kurt Aikens
Title: Assistant Professor of Physics

TABLE OF CONTENTS

TABLE OF FIGURES

Chapter 1

INTRODUCTION

1.1. Overview

This thesis deals primarily with the design of the corners of the Houghton College wind tunnel. Section 1.2 presents a brief overview of the history of experimental fluid dynamics, Section 1.3 discusses the different modes of how to solve fluid dynamics problems, section 1.4 focuses on the use of corners in a wind tunnel, and Section 1.5 discusses the objective of the present research. The evolution of the uses of wind tunnels will be presented and their usefulness shown, thereby providing motivation for building a closed-return wind tunnel and why the design of the corners is important.

1.2. History of Experimental Fluid Dynamics

Since the work of pioneers of the study of aerodynamics, like the Wright brothers, engineers and scientists have desired a more accurate understanding of the effect of fluid flows on various objects. Early researchers of the field, like Benjamin Robins, sought experimental approaches for improving understanding. Robins (1707 – 1751) began his research using a whirling arm, and he is considered to be the first to implement such technology. His work was foundational in the early study of experimental aerodynamics [1]. Figure 1 shows a sketch of Robins' whirling arm mechanism. The whirling arm used falling weights with a pulley and spindle system to generate wind speeds of only a few feet per second [1]. As the weight falls, it unwinds the spindle causing the arm and test object to accelerate.

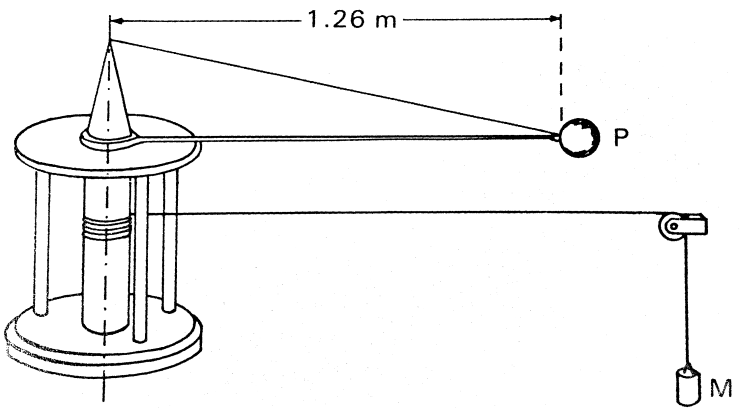

Figure 1. Diagram of Benjamin Robins' whirling arm. The model, *P*, is held approximately 4 feet from the center on the arm of the machine. The model is spun by the falling mass, *M,* acting upon the pulley-spindle system. The model was able to reach speeds of a few feet per second. Figure taken from Ref. [1].

Research with the whirling arm continued throughout the rest of the nineteenth century with other researchers like Sir George Cayley (1773 – 1857), who allegedly built the first successful unmanned glider. Cayley was also one of the first researchers who realized that forward motion of a wing could generate an upward force. By the end of the nineteenth century, most aerodynamic measurements had been made using a whirling arm. Such data was not without its faults, however. For example, the rotation of the arm and tested object cause both to move through their own wakes [1].

Wind tunnels were later developed in the late nineteenth century, and proved to be superior to whirling arm set-ups. Wind tunnels allowed researchers to have more controllable airstreams in which a test model could be placed and studied. Creation of the wind tunnel made it much easier to study basic forces on an aircraft during flight [1].

At the turn of the twentieth century, the Wright brothers were beginning their work on the world's first successful manned glider. The brothers based their initial calculations on Lilienthal's measurements of lift and drag coefficients [2] which were later organized and published in table format [3]. After their second unsuccessful glider test, they were if the data that they had based their design on was correct. The brothers set out to collect their own measurements. In their first method of testing, they mounted models to the front of a bicycle and rode it up and down a road to observe how the models reacted to the high speeds. Their findings using the bicycle method affirmed their suspicions that the existing tables, mentioned previously, were not as accurate as they wanted them to be. To obtain more accurate results, they built a small wind tunnel powered by an internal combustion engine [1]. A sketch of their wind tunnel is shown in Figure 2.

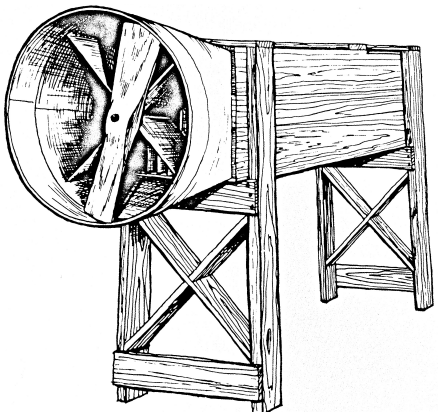

Figure 2. A sketch of the Wright brothers' first wind tunnel. The test section of the wind tunnel had a square cross section. It was powered by an internal combustion engine and positioned the blades of the fan upstream of the model being tested. Pleased with the results of their tests with this tunnel, the brothers later built a larger version of the same tunnel. Figure taken from Ref. [1].

There are two basic classifications of wind tunnels: open circuit, like the Wright brothers' tunnel, and closed circuit. An open circuit wind tunnel pulls air from and exhausts it to the room it is in without any predetermined path for returning the air from the exit to the entrance. A closed circuit wind tunnel, on the other hand, continuously recirculates air in a predetermined path (the tunnel) with little to no mixing with outside air [4]. For similarly sized test sections, both types of tunnels have their advantages and disadvantages. Generally, the construction cost of an open circuit wind tunnel is much lower than that for a closed circuit tunnel. However, they tend to be louder than closed-return tunnels and they need to be placed far away from walls to promote a uniform inflow to the tunnel. This further limits their maximum allowable size when they are located in small rooms. In contrast, closed circuit wind tunnels produce less noise, they are capable of operating in smaller rooms, and they can have better quality of flows [4].

The varieties of different wind tunnels that have been designed and used reflect the array of problems that they are used to study. They can be designed to test how models react in free flight, under icing conditions, to study the noise generated by a flow and how to best suppress it, or even to observe the effects of a moving wheel on a car while driving [5].

1.3. Methods of Fluid Mechanics

Because of the wide variety of fluid problems to be solved, there is similarly a variety of ways to solve these problems. The focus here is on experimental approaches to fluid dynamics but there are two alternative approaches: analytical fluid dynamics and computational fluid dynamics (CFD). The advantages and disadvantages of these compared to experimental methodologies are considered next.

Studying fluids through an analytical approach, when possible, is primarily useful when the exact solution to a fluid problem can be found. This is obviously useful since having an exact solution allows any characteristic to be observed at any point in space and time. Unfortunately there are only tens of known exact solutions for fluid problems, and they often require simplifying assumptions and have fairly simple geometries. For example, there is an exact solution for incompressible laminar flow through an infinitely long pipe [6]. With experimental methods, far more complex problems can be studied. For example, For example, one may wish to study how air flows over a car at high speeds or how large gusts of air affect the tallest buildings in New York City. No analytical solutions exist for such cases.

In CFD, the problem geometry is recreated in computer software and flow solutions are approximated through simulation. This method may be used to reduce project cost, since simulations are often less expensive than experiments and results can be obtained more quickly. Furthermore, simulations allow engineers to quickly evaluate many design choices because they do not require building a physical model. Therefore, CFD is particularly useful for focusing designs to a few options that can be tested experimentally. The primary downfall of CFD is that computer solutions are approximate at best. Because of the benefits of both CFD and experimental methods, they are often used together to maximize the strengths of each.

1.4. The Use of Corners in a Closed-Return Wind Tunnel

As discussed in Section 1.2, wind tunnels commonly have closed or open return systems; this dictates how they recirculate air. Closed return wind tunnels have corners and are

closed off to the outside environment so that the air is circulated within the wind tunnel. The present work is concerned with closed-return wind tunnels which have two common designs for corners – both are shown in Figure 3. The first is that of a continuously curved tube, and the second utilizes rectangular corners. It is important to note that there are many variations of these shapes in tunnels with rectangular tubing, circular tubing, and the same for the corners. Rounded corners are generally capable of having lower losses than rectangular corners [7]. However, they also take up more space and are more complicated to build than their rectangular counterparts. Rectangular corners will be used in the Houghton College wind tunnel.

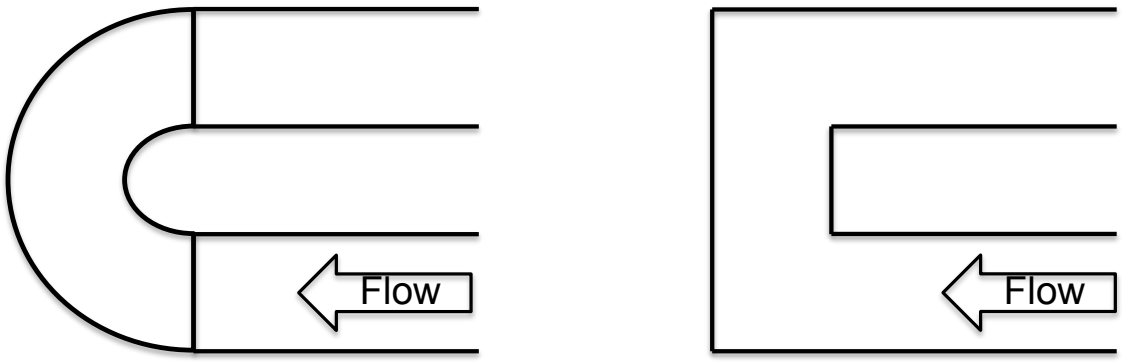

Figure 3. A basic depiction of round and rectangular wind tunnel corners. The image to the left represents a round corner of constant area and that on the right is a rectangular corner with constant area [4].

Corners are important since there is potential for large energy loss as the fluid flows around the corners. Therefore, the maximum efficiency of the corners is sought. For rectangular corners, turning vanes are necessary to improve efficiency. A turning vane changes the direction of airflow inside a duct and often includes a curved panel portion with a leading edge and a trailing edge [8]. To achieve the best efficiency with turning vanes, a variety of things are required: efficient vane cross-sectional shape, proper

alignment of the vanes with the flow, and proper spacing between the vanes. If implemented properly, vanes can reduce the losses of pressure from the inflow to the outflow observed in the corners of the wind tunnel [9] and promote flow uniformity [10]. The change in pressure from the inflow to the outflow is called stagnation pressure.

In general, there are two types of turning vanes which are pictured in Figure 4: single wall and double wall. As the names suggest, a single wall turning vane is one that has one wall and is typically in a shape resembling a quarter of a circle. Double wall vanes have two walls, giving them an airfoil shape. Turning vanes with an airfoil cross-section can be more efficient, and are better equipped to handle fluid flows at different incoming angles [4].

As mentioned, turning vanes decrease energy losses (i.e., stagnation pressure losses) in tunnel corners. To provide an idea of the magnitude of this reduction in losses, results from Krober [11] are discussed next. In his experiments, the velocity of the fluid in the corner was 28 m/s (62.63 mph), the Reynolds number based on the chord length of the vanes was 110,000, and the chord length was 59.3 mm (2.33 in.) [11]. The original reference reports a Reynolds number of 40,000, but it is not clear how that is calculated. The ratio of the diagonal spacing between vanes to the vane chord length was about 0.48, implying that the horizontal spacing was 0.34. It was found that stagnation pressure losses were reduced by 92% when two different single wall vane profiles were introduced into their rectangular corners -- a significant loss reduction. It is also important to note that there have been many studies on the spacing of single wall turning vanes in corners of wind tunnels, but comparatively fewer on the spacing of double wall turning vanes. Since it is expected that the optimal spacing is a function of the vane profile that is used, the goal of the present

work is to determine the optimal number of turning vanes for the specific vane profile and corner geometries of the Houghton College wind tunnel.

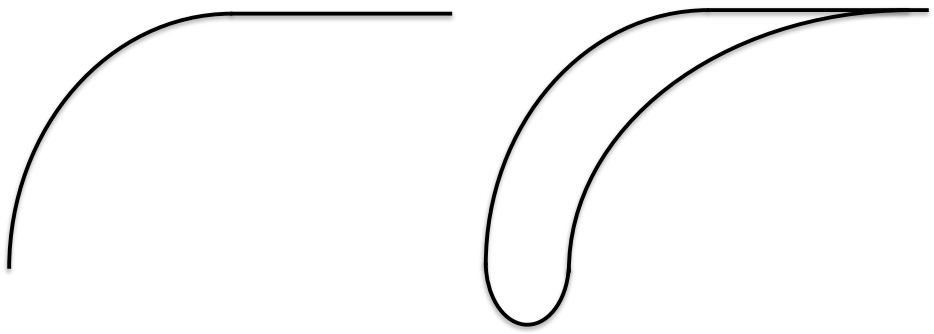

Figure 4. Depictions of single and double wall turning vanes are shown. Fluid would flow from the bottom of theis figure and exit to the right side of the page. On the left is a single wall turning vane, comprised of a quarter circle with an extended tail on the trailing edge. The right shows a double wall turning vane, which has a similar cross-section to an airfoil.

1.5. Objective of Project

As mentioned in previous sections, analytic and computational approaches to solving fluid dynamics problems are never sufficient by themselves. Because of this, the Houghton College physics department is designing and building a low-speed closed-return wind tunnel. This wind tunnel will allow a variety of experiments to be performed including tests on aircraft models with ice build up, basic flow visualization, and more. It will also enable students to perform laboratory experiments in fluid dynamics courses.

The work discussed in this thesis is primarily focused on the design of the four corners for the Houghton College closed-return wind tunnel. The general design and dimensions of the corners of the wind tunnel were chosen by Jonathan Jaramillo [12]. The main goal of this work is to determine the optimal number of turning vanes for each of the corners. CFD is

used for this purpose to compare simulation data of the corner geometries with different numbers of turning vanes placed along the corner's diagonal.

Chapter 2

THEORY

2.1. Governing Equations and Flow Field Properties

CFD programs are designed to approximate the solution to the governing equations of fluid dynamics. In this work, it is assumed that the air obeys the ideal gas law and has constant specific heat. The governing equations can be written in differential form as

$$\frac{\partial}{\partial t}(\rho) + \frac{\partial}{\partial x_i}(\rho v_i) = 0 \tag{1}$$

$$\frac{\partial}{\partial t}(\rho v_i) + \frac{\partial}{\partial x_j}\left(\rho v_i v_j + \delta_{ij} p\right) = \frac{\partial}{\partial x_i}\left(\tau_{ij}\right) \tag{2}$$

$$\frac{\partial}{\partial t}(\rho e_t) + \frac{\partial}{\partial x_i}(\rho e_t + p v_i) = \frac{\partial}{\partial x_i}(v_j \tau_{ij} - q_i) \tag{3}$$

where ρ, v_i, p, and e_t are the fluid density, velocity in coordinate direction i, pressure, and the total energy per unit mass of the system, respectively. Also, in Equations (1) through (3), q_i is the heat flux, and δ_{ij} is the Kronecker delta function. Additionally, we require fluids to obey the equation of state,

$$p = \rho R T. \tag{4}$$

This is the ideal gas law where R and T are the ideal gas constant divided by the molar mass of air, and the absolute temperature, respectively. Equations (1) through (3) are written with Einstein's summation convention where repeated indices indicate that the

term is summed over all possible values of the index. The equation for total energy of the system is given by

$$\rho e_t = \frac{p}{\gamma - 1} + \frac{1}{2}\rho v_i v_i \tag{5}$$

where γ is the ratio of specific heats for the given fluid (c_p/c_v). Equations (1) through Equation (5) are commonly referred to as the Navier-Stokes equations. Additionally, the viscous stress tensor shown in Equation (2), τ_{ij}, is defined as

$$\tau_{ij} = \mu\left(\frac{\partial v_i}{\partial x_j} + \frac{\partial v_j}{\partial x_i} - \frac{2}{3}\frac{\partial v_k}{\partial x_k}\delta_{ij}\right) \tag{6}$$

where μ is the dynamic viscosity. The dynamic viscosity is a function of temperature and can be modeled by Sutherland's law

$$\mu = \mu_0\left(\frac{T}{T_0}\right)^{3/2}\frac{T_0 + T_{\text{Suth}}}{T + T_{\text{Suth}}} \tag{7}$$

where μ_0 is the reference viscosity of air at the reference temperature T_0 and $T_{\text{Suth}} = 110.4$ K.

A more useful form of the governing equations can be obtained by non-dimensionalizing them. For this purpose, we will non-dimensionalize the variables by the chosen quantities $\rho' = \frac{\rho}{\rho_\infty}$, $v' = \frac{v}{v_\infty}$, $p' = \frac{p}{\rho_\infty v_\infty^2}$, $x' = \frac{x}{L}$, and $t' = L/v_\infty$. Primed quantities are dimensionless, a subscript infinity designates a reference quantity, and L is the reference length. Then it follows that the governing equations can be represented as

$$\frac{\partial}{\partial t'}(\rho') + \frac{\partial}{\partial x_i'}(\rho' v_i') = 0 \tag{8}$$

$$\frac{\partial}{\partial t'}(\rho' v_i') + \frac{\partial}{\partial x_i'}(\rho' v_i' v_j') = -\frac{\partial p'}{\partial x_i} + \frac{1}{Re}\frac{\partial}{\partial x_i}\left(\left[\mu'\left(\frac{\partial v_i'}{\partial x'} + \frac{\partial v_j'}{\partial x'} - \frac{2}{3}\frac{\partial v_k}{\partial x_k}\delta_{ij}\right)\right]\right) \quad (9)$$

$$p' = \frac{\rho' T'}{\gamma M^2}. \quad (10)$$

The Mach number is defined by

$$M = \sqrt{\gamma RT} \quad (11)$$

and the Reynolds number is defined by

$$Re = \frac{\rho_\infty v_\infty L}{\mu} \quad (12)$$

where ρ_∞, v_∞, L, and μ are the reference fluid density, fluid velocity, length of the geometry of concern, and the viscosity of the fluid, respectively [13].

At low Mach numbers, it can be shown that the only relevant parameter to the calculation is the Reynolds number. Therefore, for a given flow problem, the non-dimensional solution only depends on one parameter instead of multiple (e.g., ρ_∞, v_∞). This quantity is often useful so that two distinctly different flow fields can be compared if they are dynamically similar. Fluid flows, in many cases, may be considered dynamically similar if the bodies and solid boundaries are geometrically similar and the Reynolds number and Mach number for the two flows are the same [13]. Because of this, experiments can be done on much smaller systems that are dynamically similar to the full-scale models of the desired geometry, thereby dramatically reducing costs. A trivial example of this is shown in Figure 5. It is clear that both systems have geometrically similar bodies, have equivalent flows around the geometry and equivalent Reynolds and Mach numbers. Because of this, the non-

dimensional solution would be quantitatively the same for each flow, implying that v/V_1 would be the same as v/V_2 at the same non-dimensional location and time.

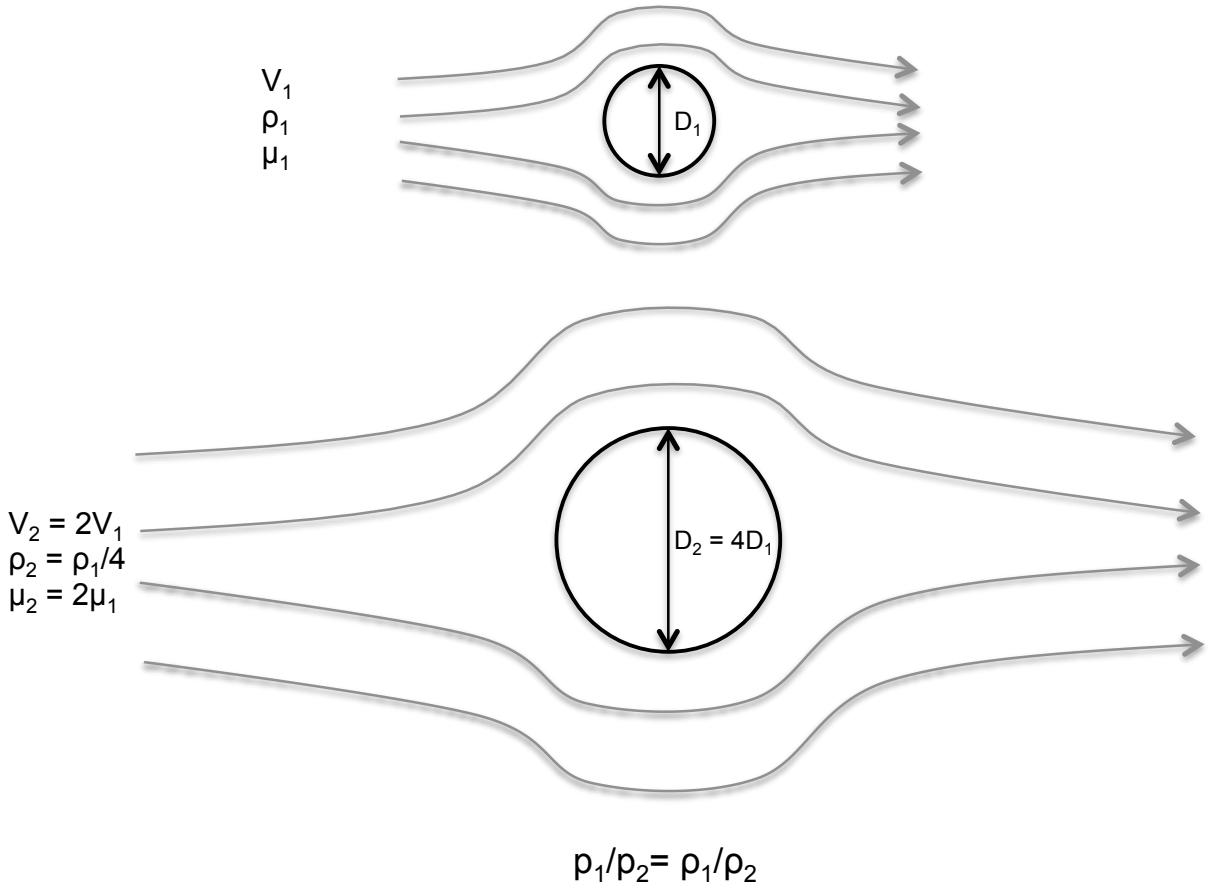

Figure 5. Flow similarity depicted between dynamically similar geometries. The Mach and Reynolds numbers are the same for both geometries: see Equations (11) and (12). Additionally by the ideal gas law, pressure and density must be in the ratio $\frac{p_1}{p_2} = \frac{\rho_1}{\rho_2}$. This is often difficult to replicate in experiments because it requires different fluid densities, viscosities, and pressures, while the temperature is held constant at the same temperature as the first experiment.

2.2. Computational Fluid Dynamics

To have a general understanding of CFD, we must discuss the methodologies used to approximately solve the Navier-Stokes equations in the previous section. There are many different numerical methods in the field of CFD, but we will only discuss the finite volume method, as this is the method that ANSYS Fluent, a CFD software, uses to approximate solutions for fluid flows. The finite volume method is used in many commercial CFD programs, and it is very popular because of its ability to use unstructured grids [14]. It can be advantageous to use unstructured meshes because they allow flexibility when it comes to grid refinement: regions of interest can easily be refined while less important areas can be meshed with larger cells. Therefore, it is often much easier to make high quality unstructured meshes for practical engineering problems. Figure 6 illustrates what an unstructured mesh might look like for the problem of fluid flowing over a flat plate.

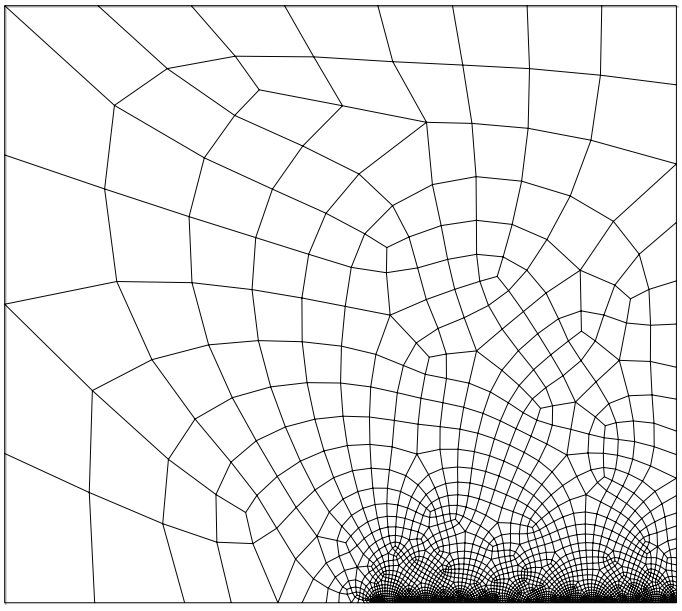

Figure 6. An unstructured mesh for the problem of fluid flowing over a flat plate. The plate is at the bottom right where the density of cells is higher and each cell is smaller.

More often than not, there are not known exact solutions for the governing equations for particular fluid flows. Therefore, the solution must be approximated. To do so, the solution is found using the governing equations in their integral form. In the finite volume method, each of Equations (8) through (10) can be written in the following general form

$$\frac{d}{dt}\int_{\Omega} \Phi d\Omega = -\int_{S} \Phi \boldsymbol{V} \cdot \boldsymbol{n} dS + \int_{S} \mathcal{X} \nabla \Phi \cdot \boldsymbol{n} dS + \int_{\Omega} Q d\Omega \,, \tag{13}$$

where Φ is the flux through the cell boundary, Ω is an arbitrary control volume with bounding surface S, normal vector $\boldsymbol{n}$, and Q is intensity per unit length. The left-hand side represents the rate of change of the amount of Φ in Ω. $-\int_S \Phi \boldsymbol{V} \cdot \boldsymbol{n} dS$ represents convective fluxes through the surface S and $\int_S \mathcal{X} \nabla \Phi \cdot \boldsymbol{n} dS$ represents diffusive flux terms like viscous friction and heat conduction. Note that $\mathcal{X}$ is a constant or variable coefficient of diffusion. Lastly, $\int_\Omega Q d\Omega$ is a source term – it represents the change in Φ by intensity Q per unit volume.

When simulating a fluid flow, the fluid flow in a given domain can be broken into small pieces, or discretized, so that the equation can be applied to each piece of the total volume. The discretized domain is referred to as a "mesh" or "grid". A simple example of a cell like this is shown in Figure 7.

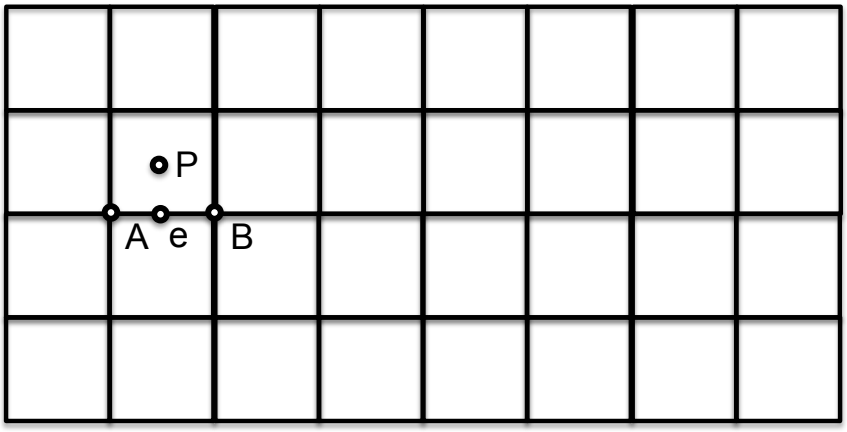

Figure 7. Illustration of a discretized flow domain. Each volume has a cell-centered grid point, like point P. The approximate solution for Equation (13) is sought at P and in each cell. S_{AB} Is the length between points A and B, or the width of the cell. Point e is the midpoint of side AB.

To approximate the solution of the volume integral, the integral is replaced with the product of the cell's volume, $|\Omega|$, and the mean value of the quantity, $\overline{\Phi}$. Then it follows that the approximation of the volume integral for point P in Figure 7 is

$$\int_{\Omega} \Phi d\Omega = \overline{\Phi}|\Omega| \approx \Phi_P|\Omega|. \tag{14}$$

The integral approximation is second order with respect to the dimensions of the cell, i.e. $O\ (\Delta x^2, \Delta y^2)$. As the cell size gets smaller the approximation gets better. Additionally the surface integral is accounted for by taking the product of the average flux at the border of a two-dimensional cell, $\bar{f}$, the approximate value of the integrand at point P, f_P, and its length,

$$\int_{AB} f dS = \bar{f} S_e \approx f_P S_e, \tag{15}$$

and the approximation error is on the order of the square of the length of the cell, S_{AB}. Since the value of the fluid variables are only known at the center of the cells, the value of the

fluxes between cells is interpolated at the cell interfaces. Lastly, the time integration is completed using numerical methods for ordinary differential equations.

The finite volume method discussed above can be generalized to less structured and more arbitrary shapes and can be used to achieve higher orders of accuracy. In many ways, this is an interesting problem to study on its own. For example, researchers at NASA Glenn Research Center have developed a CFD program that allows for an arbitrary order of accuracy to be used for the solver [15]. This method is closer to a finite element method than a finite volume, and provides a higher accuracy for simulations.

2.3. Related Flow Phenomena

In order to understand flow phenomena that occur in the corners of a wind tunnel, it is important to understand different types of fluid flows. Firstly, consider the nature of the fluid flow itself. The fluid of interest can be classified as inviscid or viscous. An inviscid fluid is one that has negligible viscosity, or more simply, has negligible frictional effects. A viscous fluid is affected by friction on solid surfaces, resulting in what is known as the no-slip condition [16]. Additionally, consider incompressible and compressible flows. An "incompressible" fluid flow is where density can be assumed to be constant. Fluid flows where the density can vary in space and time are called "compressible" [13].

The no-slip condition occurs near the surface of a solid object, where the frictional force causes the flow velocity to be zero, as depicted in Figure 8. In general, this boundary condition is applied to fluids near solid surfaces, like the walls of a pipe or an airfoil. It also follows that very close to the surface there is a thin region where the velocity of the fluid increases very rapidly at further distances from the wall. This is also shown in Figure 8 and

is referred to as the boundary layer. A boundary layer is the region where the fluid velocity has been reduced due to the presence of a wall [13]; pictures of boundary layer from experiments are shown in Figure 9.

In CFD, boundary conditions are used to constrain the physical attributes of fluid flows and the surfaces over which they flow. For example, it might be desirable to hold inflow velocity into a pipe at a constant velocity or give a specific velocity profile [17]. In order to apply boundary conditions, one must first understand some related flow phenomena such as laminar flow, turbulent flow, and flow separation. Boundary conditions have a major effect on the stability and convergence of computer simulations, and are in fact necessary for boundaries of finite geometries since it is often difficult to observe the full flow due to the limited memory of computers [18].

Laminar flow and turbulent flow stand in stark contrast to one another. When following the path of the flow, a laminar flow exhibits a smooth path while a turbulent flow has a more chaotic pattern of motion [13]. Figure 9 shows experimental pictures of a laminar and turbulent flow over a small bump. Due to the chaotic motion of the fluid, turbulent flows have a higher average flow velocity near solid surfaces than laminar flows, as shown in Figure 8, and therefore have higher frictional losses [13].

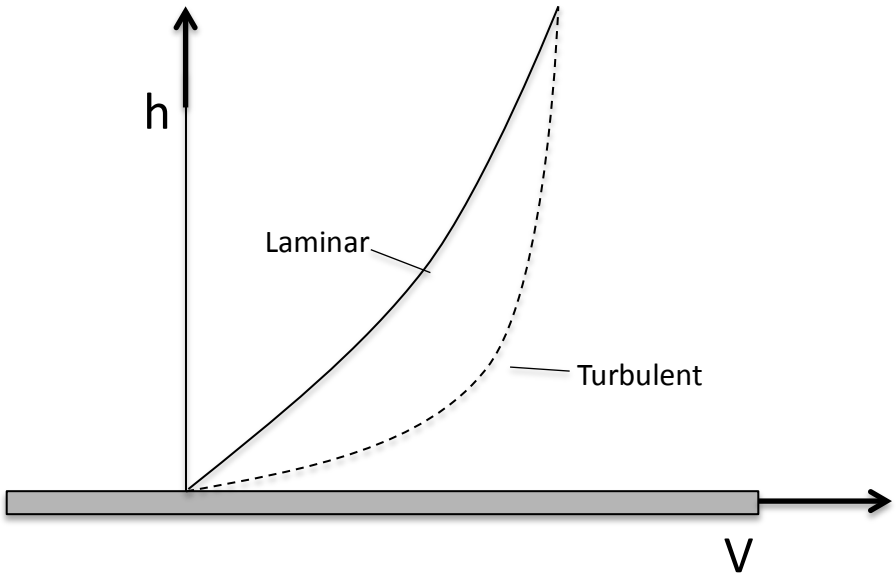

Figure 8. A comparison of laminar and turbulent velocity profiles. The flow is from left to right over a flat plate in this example. Note that h is the height away from the wall and V is the average streamwise velocity of the fluid at the corresponding height. This figure could also be thought of as a visual representation of how far fluid particles have traveled from the h axis over a given time, t. Figure adapted from Ref. [4].

Boundary layers, as discussed, form along solid surfaces. They do not always remain attached to them, however. In some cases, a flow can become separated from the walls and become stagnant or mix with itself instead of moving with the rest of the fluid. Flow separation occurs when fluid near solid surfaces experiences a pressure gradient in the direction opposite of the fluid flow [13]. Similar to turbulent flow, slowed fluid and small eddies can be observed near the wall and in some cases in the body of the fluid. Figure 10 shows a separated flow with eddies in the region of separation. When the fluid flow has separation, some of the eddies in that region are even larger those in a typical turbulent boundary layer. This can cause the fluid to flow backwards and can even cause the fluid to flow backwards near the wall or surface over which the fluid is flowing [16]. Separation is relevant to wind tunnel design because it causes large losses of stagnation pressure.

Therefore, good tunnel designs avoid it. With all of these characteristics in mind, it is possible to analyze the behavior of air in the corner of a wind tunnel.

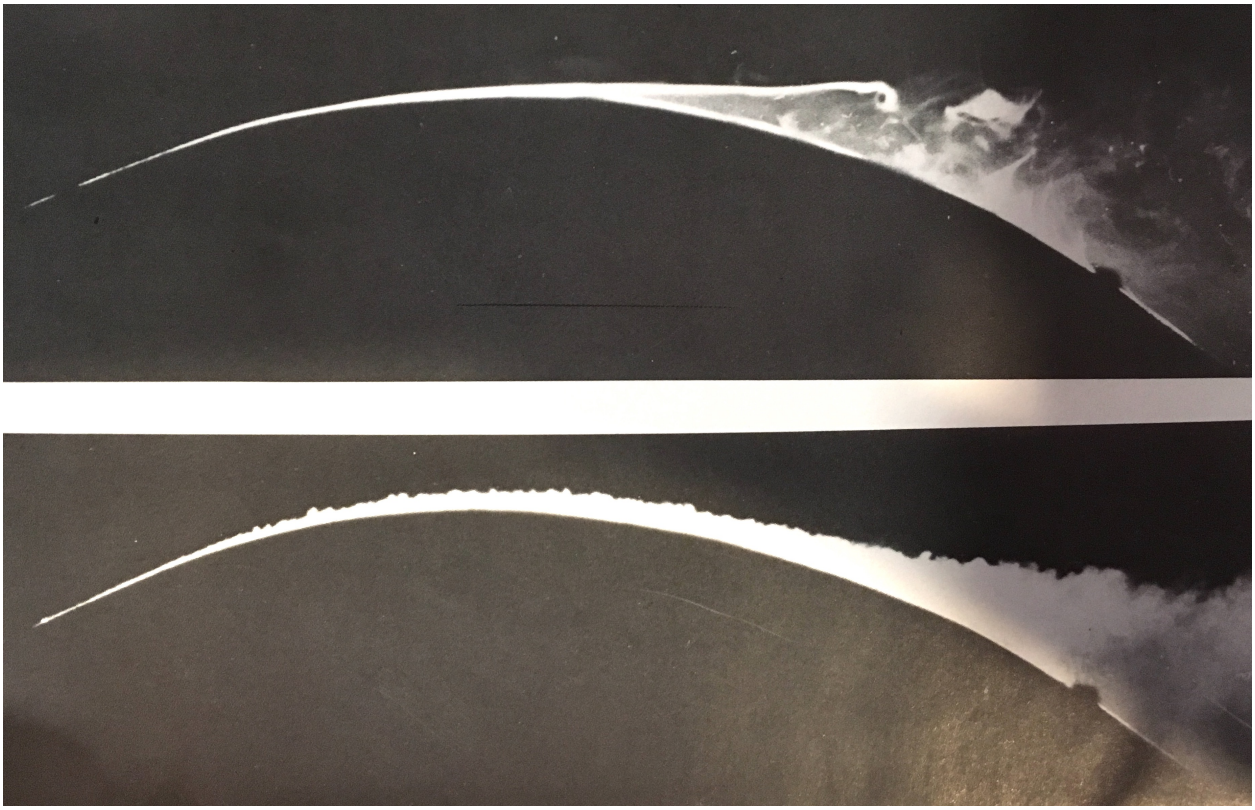

Figure 9. A picture of a boundary layer as it develops over the top of a convex surface. Titanium tetrachloride is placed on the model surface at the beginning of the model. As the fluid flows to the right, the boundary layer grows thicker. The effects due to the wall are lessened the farther away from the surface (floor) the fluid gets until it reaches the free-stream velocity. Notice that in the top image, the laminar flow has a smooth path for the first half of the image, while the turbulent path in the bottom image is much more chaotic and unpredictable. Also notice that the turbulent boundary layer stays attached to the surface of the hump further downstream than the laminar boundary layer does. Image taken from Ref. [19].

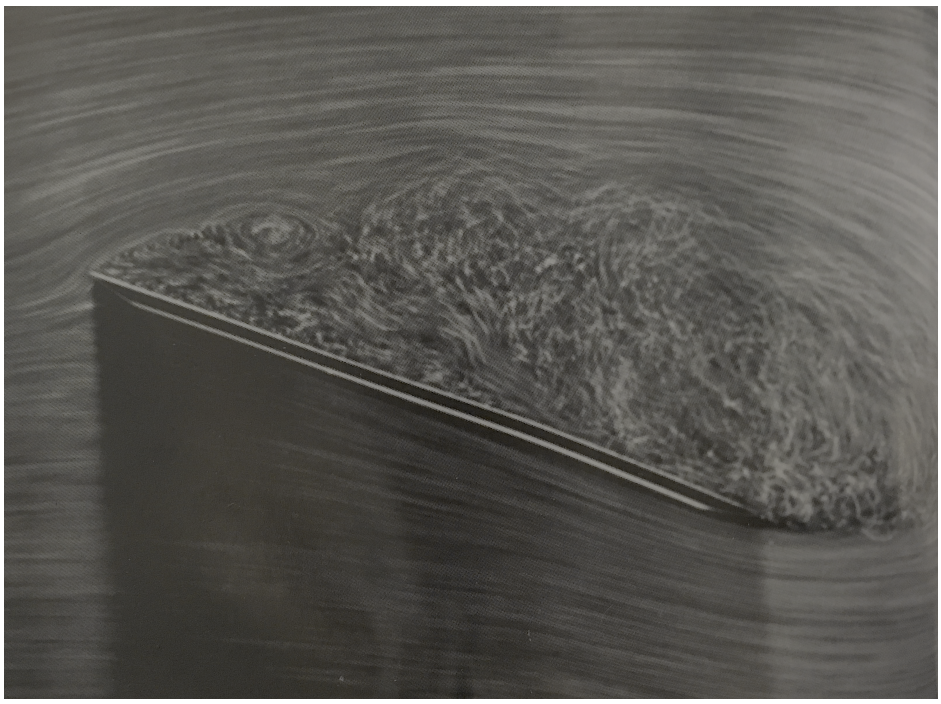

Figure 10. Photo of separation over an inclined plate. Visualization is by bubbles in water. As the fluid moves past the upper edge of the inclined plate from left to right, it is unable to remain attached to the surface of the plate due to the adverse pressure gradient there. The separation region is visible due to the chaotic eddies that separate it from the smooth streamlines of the freestream flow elsewhere in the image. Figure taken from Ref. [19].

2.4. Corner Loss Coefficient

Since air is viscous, there is observable energy loss throughout each section in a wind tunnel. In prior work on the Houghton wind tunnel, these losses were estimated using empirical loss estimates for a maximum air speed in the test section of 44.7 m/s (100 mph) [12]. More detailed calculations are required here for the corners.

Losses in the corners of the wind tunnel may be reduced in two ways: selecting an efficient turning-vane shape and choosing the corresponding optimal chord-to-gap ratio [4]. To compare various choices, the non-dimensional corner loss coefficient is calculated as

$$K_c = \frac{\Delta H_c}{q_c} = \frac{p_i + \frac{1}{2}\rho U_i^2 - (p_0 + \frac{1}{2}\rho U_0^2)}{\frac{1}{2}\rho U_i^2} \tag{16}$$

where ρ is the fluid density, p_i is the inflow pressure of the corner, $\frac{1}{2}\rho U_i^2$ is the kinetic energy term at the inflow, and p_0 and $\frac{1}{2}\rho U_0^2$ are the pressure and kinetic energy at the outflow [4]. ΔH_c is the change in stagnation pressure and q_c is the dynamic pressure (or kinetic energy per unit volume) in the corner. Stagnation pressure is not constant in this case since energy is not conserved as the flow travels around a corner. To provide an idea of the possible range of values, a corner without turning vanes can have an observable loss of $K_c \geq 1$ [4]. If the appropriate chord-to-gap ratio is chosen along with well-designed corner vanes, a loss coefficient of $K_c \leq 0.10$ can be observed [4]. Assuming that the flow is incompressible, steady, and moves perpendicular to the inflow and outflow surfaces, it follows from the continuity equation (Equation (1)) that the area-weighted average velocity is the same at the inlet and the outlet. Therefore, Equation (16) can be simplified to

$$K_c = \frac{p_i - p_0}{\frac{1}{2}\rho U_i^2}. \tag{17}$$

Utilized in the initial design of the wind tunnel, the empirical curvefit for losses in corners is given by [4]

$$K_c \approx 0.1 + \frac{4.55}{(\log_{10} Re_c)^{2.58}} \tag{18}$$

where Re_c is the Reynolds number based on the turning vane chord length.

When designing corners, one must choose which type of turning vane to use. Shown in Figure 4 are two of the three most common types: a constant-radius arc with a longer trailing edge and a double wall turning vane. The third common type is a constant-radius

arc that is a quarter of a circle but does not include an elongated trailing edge. To provide an idea for typical loss coefficients for various turning vane arrangements, various studies are reviewed [20,21]. For additional information, Patterson provides an early review of work completed on tunnel corner design [7]. Klein et al. and Collar tested single wall turning vanes and double wall turning vanes, which are similar to those used in the current study. In Ref. [21], the Reynolds number was reported to be approximately $4 \cdot 10^4$ based on the mean velocity in the duct and vane chord length. Klein et al. also conducted detailed studies of the spacing between turning vanes, where they reported that the optimal horizontal gap-to-chord ratio to be between 0.3 to 0.5. Collar's study [20] focused on using the same arrangement of turning vanes for varying Reynolds numbers. The horizontal gap-to-chord ratio was 0.6 and the Reynolds number ranged from 50,000 to 180,000 [20].

Klein et al. found that single wall turning vanes were favorable in their experiment instead of double-walled vanes [21]. They measured a loss coefficient of 0.2 for a single wall vanes and 0.25 for double wall vanes similar to the one used in the present work [21]. While this is not the expected trend, it is unclear how this might have occurred in their study. The authors also report that the difference between using single and double-wall turning vanes is not so significant [21]. The most important observation to take away in this circumstance is that it is important to have some sort of turning vanes, so long as they have a reasonable profile. Collar, on the other hand, found that turning vanes similar to those utilized here experience a loss coefficient of approximately 10 percent for $Re_c = 5 \cdot 10^4$ which further drops to 7 percent at $Re_c = 9 \cdot 10^4$ [20].

The shape of the vanes bought for the current project are similar to the shape of vane "number 6" used by Klein et al. [21] and "Section C" used by Collar [20], and they are commercially distributed by Aero Dyne. The vanes were purchased prior to the beginning of this research, and were therefore used in simulations for designing the corner vane array. A technical drawing of the utilized turning vanes is shown in Figure 11. An additional benefit of buying double-wall turning vanes is that they are easier to mount in corners. This is especially true for the vanes used in this project because of their included mounting holes.

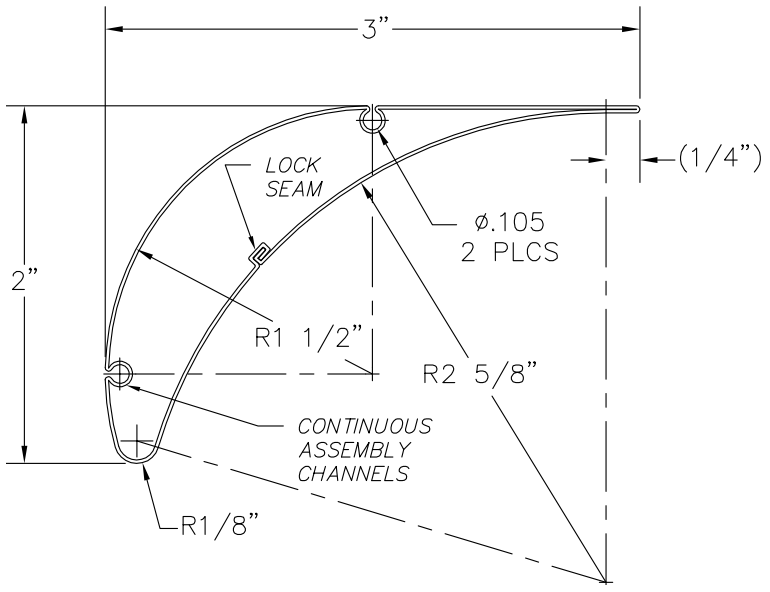

Figure 11. A two-dimensional drawing of the turning vanes used in the corners. Aerodyne HVAC turning vanes are used since they may have lower overall loss coefficients for some vane spacings compared to single-wall vanes and they are commercially available.

Chapter 3

EXPERIMENT

Chapter 3 discusses the details of the numerical experiments used to determine the optimal turning vane spacing for the Houghton College wind tunnel. Section 3.1 deals with the general design of the wind tunnel, Section 3.2 discusses mesh generation and refinement, and Section 3.3 includes details about the boundary conditions and other simulation settings.

3.1. Houghton College Wind Tunnel Design

The wind tunnel at Houghton College will be a low-speed closed-return wind tunnel. A three-dimensional rendering of the wind tunnel is shown in Figure 12. Starting at the acrylic test section (top middle) and going in the direction of the flow, the wind tunnel consists of a test section, diffuser one, corner one, corner two, transition one, the fan, transition two, diffuser two, corner three, corner four, a settling chamber and a nozzle before returning to the test section. In general, the important dimensions are that the wind tunnel will fit inside a unistrut frame that is roughly 4.57 meters long by 1 meter wide by 2 meters tall [12]. Corners one and two have a cross sectional area of 0.4826 m by 0.4826 m, and corners three and four have a cross-sectional area of 0.6223 m by 0.6223 m.

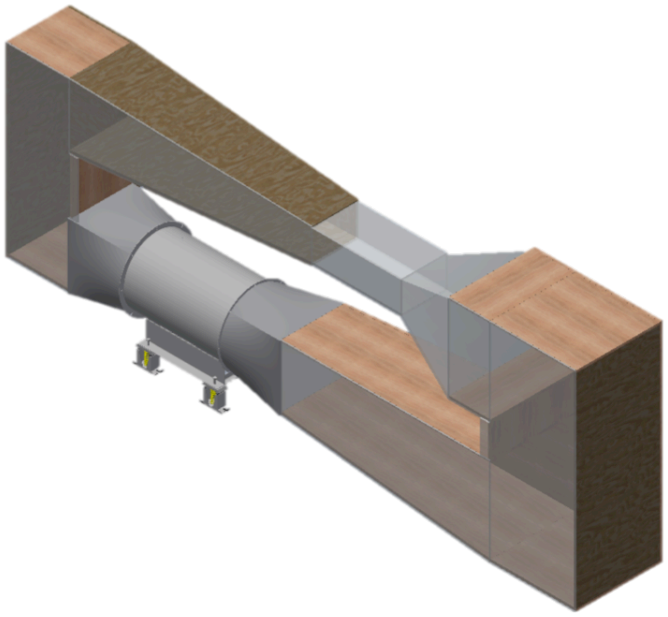

Figure 12. A digital rendering of the Houghton College wind tunnel. The test section (top middle) is made entirely of acrylic, as is one side of the tunnel. The direction of flow is counterclockwise in the orientation shown.

3.2. Mesh Generation and Refinement

As stated before, empirical correlations for the loss in each component of the wind tunnel were utilized for its general design. However, there are some components that require more detailed design work such as the nozzle and the corners. To determine how many turning vanes are needed in each corner, their geometries were recreated in Autodesk Inventor. Different fluid geometries were created with differing numbers of equally-spaced turning vanes. This was achieved by creating an array of vanes whose spacing was controlled by an equation that was a function of the number of vanes desired. Note that all simulations were performed in two dimensions for increased efficiency (lower cost) and because of the relatively large depth of the corners. If three-dimensional simulations were run, the only part affected would be the flowfield near the walls. After the geometry was completed, it was exported as an .igs file and imported into the ANSYS Meshing software to

be meshed. Before meshing, a refinement region of approximately 2.5 times the chord length of the turnings vanes is added at the end of the turning vanes. This was added in order to further refine the region relative to the rest of the free stream flow.

Next the meshing software is used to mesh the fluid geometry. For the tunnel and vane walls, an inflation layer is applied to improve the accuracy and resolution of the predicted boundary layer and to specify how many cells are desired near the walls. Recall that the flow solution is assumed constant in each cell. This assumption obviously improves as the cells become smaller, especially in dynamic regions of the flowfield like the boundary layer. This occurs because the approximations become better when the cells become smaller. General sizing was used for the rest of the body and the refinement region behind the turning vanes was sized such that the cells in the region were smaller than those in the main body of the corner.

It was desirable to have meshes that can accurately determine the drop in stagnation pressure across each corner. Four increasingly fine meshes were created for each corner geometry ranging from approximately 5,000 cells for the coarsest grid to 75,000 cells for the finest grid. See Figure 13 for a comparison of grid refinements. Settings used for the meshes are shown in Table 1.

Grids are designed so that the first cell next to solid surfaces has a y+ value of 200 or less. See Table 1 for basic details on the final grids used for simulation. As will be discussed in the next chapter, the optimal number of vanes are determined to be 13 for corners 1 and 2 and 19 for corners 3 and 4.

Table 1. A table of settings used in making the meshes in the ANSYS Meshing software. This methodology was used for the small corners (corners one and two) as well as the large corners (corners three and four). The growth rate for the inflation layers for each mesh was 1.2. Vane End Element Size refers to the region after the end of the turning vanes that has additional refinement relative to the Body Element Size.

Grid Name	Wall Inflation Thickness (mm)	Wall Inflation Layers	Vane Inflation Thickness (mm)	Vane Inflation Layers	Body Element Size (mm)	Vane End Element Size (mm)
coarse	20	3	8	3	40	9
medium	20	6	8	6	15	4.5
fine	20	12	8	12	12.5	3
very fine	20	18	8	18	10	2.5

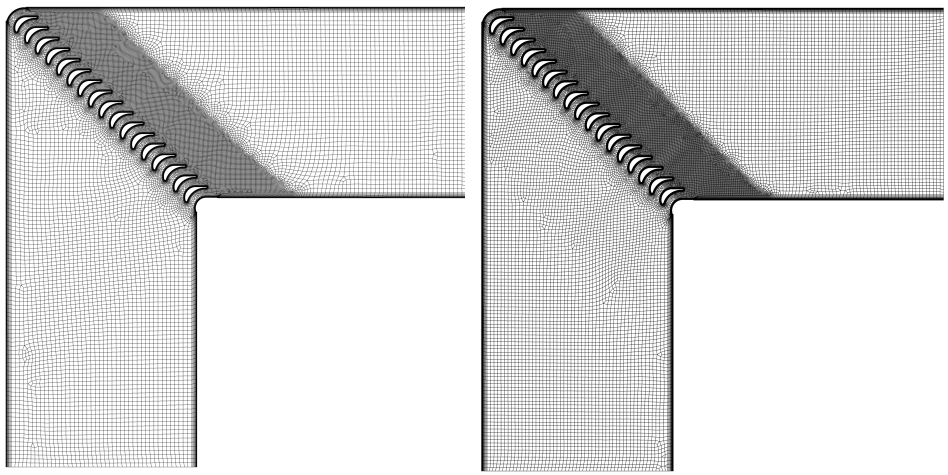

(a) (b)

Figure 13. A comparison of grid refinement for corners 3 & 4 – both have 19 vanes. (a) represents the fine mesh from Table 1 and (b) is the very fine.

3.3. Boundary Conditions and Simulation Settings

Once the mesh was made, boundary conditions must be applied so that it most closely approximates the real-world scenario that it is modeling. In this work, the outflow is

enforced to have a gauge pressure of zero and the fluid velocity at the tunnel walls and vane walls is defined to be zero. Additionally, the inlet of speed is defined to be 15.68561 m/s for corners one and two, and 8.202569 m/s in corners three and four. These are the corner speeds for the maximum designed test section speed of 44.7 m/s (100 mph) [12].

To perform the simulations, the realizable $k-\epsilon$ turbulence model is coupled with the Menter-Lechner near-wall treatment. The simulations are completed using ANSYS Fluent 17.1. The coupled solver is used, and a surface monitor is defined to the track inflow gauge pressure. Since the outflow pressure is constrained to be zero and the average velocity is the same before and after the corner, the inflow gauge pressure is equal to the stagnation pressure drop across the corner. Lastly, the solution is initialized with zero speed and zero gauge pressure. The simulation is considered to be converged once the residuals and the inflow pressure stop changing. This usually takes between 2,000 and 6,000 iterations.

Chapter 4

ANALYSIS

This chapter will present the results of the simulations of the smaller corners and the larger corners. First the pressure loss of each corner will be presented and the conclusion for the optimal number of vanes shown. Simulations were performed for many different arrangements of turning vanes across each corner. Uniform spacing between vanes is used in all cases. Initially, simulations were completed for corners 1 and 2 having 11, 16, 19, 26, and 31 vanes, to more quickly arrive at the minimum pressure loss. Initial results for corners 1 and 2 are shown in Figure 14 and the accompanying data is shown in Table 2. Notice that the results for 26 and 31 vanes are not shown because the pressure losses were approximately 114 Pa and 321 Pa, respectively.

As mentioned in Section 3.2, the meshes for each corner were refined successively to get more accurate results. Each series of results is named according to the mesh settings utilized: coarse, medium, fine, and very fine. See Section 3.2 for more details. It was decided that the "fine" grids gave the best results for the amount of time spent on each simulation. The fine grid simulations took between one and two hours to achieve convergence, on average, and the simulations using the very fine grids took on the order of four to seven hours to converge. Because of this, it was decided that the change in Δp for the additional amount of simulation time was not significant enough to warrant the extra simulation time. It was determined based on the initial data collected that the optimal number of vanes was between 11 and 19. Therefore, simulations using the fine mesh were completed for each

number of vanes in this range. Based on the results, it is clear that 13 vanes was the optimal number for corners 1 and 2. This arrangement had a gap-to-chord ratio of 0.451, which is within the range of 0.3 to 0.5, suggested by results from Klein et al. [21]. By Equation (12), the Reynolds number for corners 1 and 2 is 96,660. Therefore, by Equation (18) the empirically estimated loss coefficient is $K_c \approx 0.172$. This was used in the preliminary design of the wind tunnel. The minimum loss coefficient that is calculated using the simulation results and Equation (17) is $K_c = 0.158$, which is relatively close to the expected value from the empirical correlation. However, the actual loss coefficient could be higher or lower due to the present results not being grid independent. This is better than the results from Klein et al. [21], which achieved a loss coefficient of 0.25 for $Re_c = 4 \cdot 10^4$ and is higher than Collar's [20] experimental result of 0.07 for $Re_c = 90 \cdot 10^3$. The loss coefficients from these experiments are for similar double-wall turning vanes to those utilized presently, but they are not exactly the same. This could be partially responsible for the discrepancies. At any rate, the loss coefficient from the simulation appears reasonable compared to results reported by others.

Similarly for the large corners (corners 3 and 4), grid refinement was started at what was previously called the "fine" mesh and the lowest drops in stagnation pressure were checked with the "very fine" mesh. The results are shown in Figure 15 and Table 3. It is clear that the simulation results are not grid-independent but similar trends are noted for both grids with the same location for the minimum. Using 19 vanes is optimal for corners 3 and 4 which yields a horizontal gap-to-chord ratio of 0.416. Notice that this is very similar to that found for corners 1 and 2. Additionally, the pressure contour of corners three and four is shown in Figure 16. By Equation (12), the Reynolds number for corners 3 and 4 is

50,543. Therefore, by Equation (18) the empirical estimate of the loss coefficient is $K_c \approx 0.184$. The minimum loss coefficient that is calculated using the simulation results and Equation (17) yields $K_c = 0.182$. This again is better than the results published by Klein et al. but it is still higher than Collar's experimental data of 0.10 for $Re_c = 5 \cdot 10^4$. However, the expected Reynolds number trend is maintained in these simulations. As the Reynolds number increases, the loss coefficient decreases, which is consistent with Collar's [20] results.

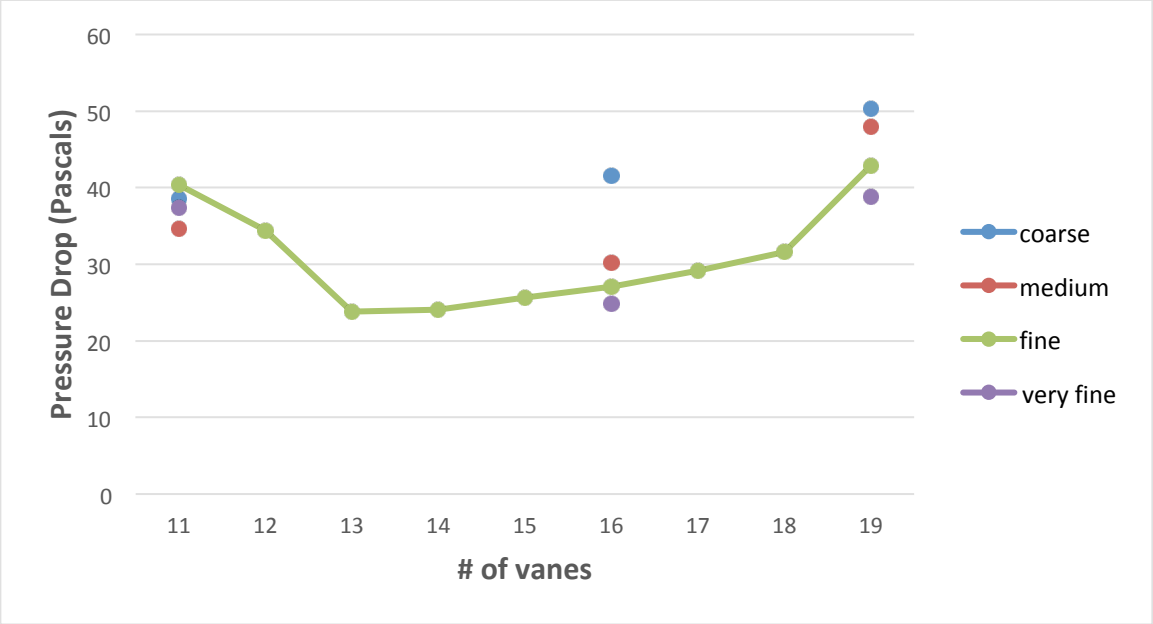

Figure 14. A plot of simulation results for the smaller corners(corners 1 and 2). The first simulations done were of 11, 16, 19, 26, and 31 vanes. Numerical values are shown in Table 2.

Table 2. Numerical values for the drops in stagnation pressure for corners 1 and 2. The pressure drop is measured in pascals. The minimum value occurs at 13 vanes across the corner.

# of vanes	11	12	13	14	15	16	17	18	19
coarse	38.59					41.50			50.34
medium	34.72					30.25			47.94
fine	40.35	34.40	23.82	24.04	25.64	27.07	29.16	31.55	42.84
very fine	37.39					24.81			38.88

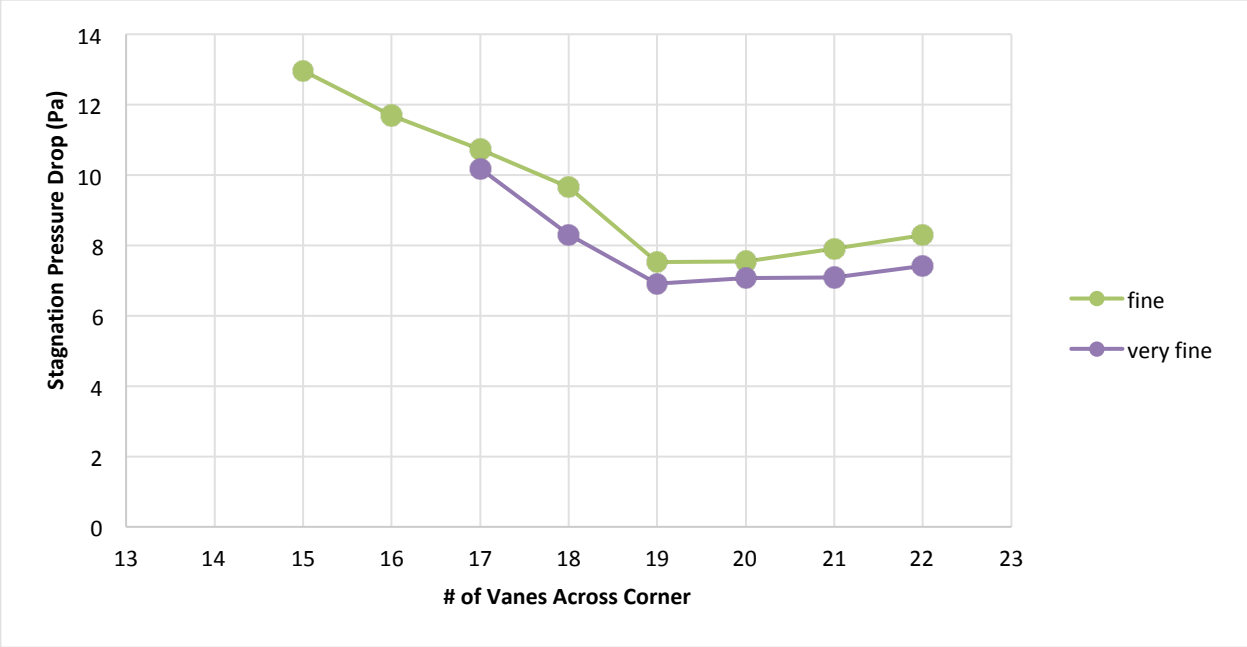

Figure 15. A plot of simulation results for the larger corners (corners 3 and 4). Numerical values are shown in Table 3.

Table 3. Numerical values for the drops in stagnation pressure for the larger corners. The pressure drop is measured in pascals. The minimum value occurs at 19 vanes across the corner.

# of vanes	15	16	17	18	19	20	21	22
fine	12.971	11.695	10.736	9.6531	7.5196	7.5497	7.9065	8.2941
very fine			10.189	8.3063	6.9134	7.0693	7.0808	7.4218

To summarize, based on the results shown in Table 2 and Table 3, the optimal number of vanes for the small corners is 13 vanes and 19 vanes is the best for the larger corners. Additionally, the loss coefficient estimates based on the simulation data for corners one and two, and three and four are 0.158 and 0.182, respectively.

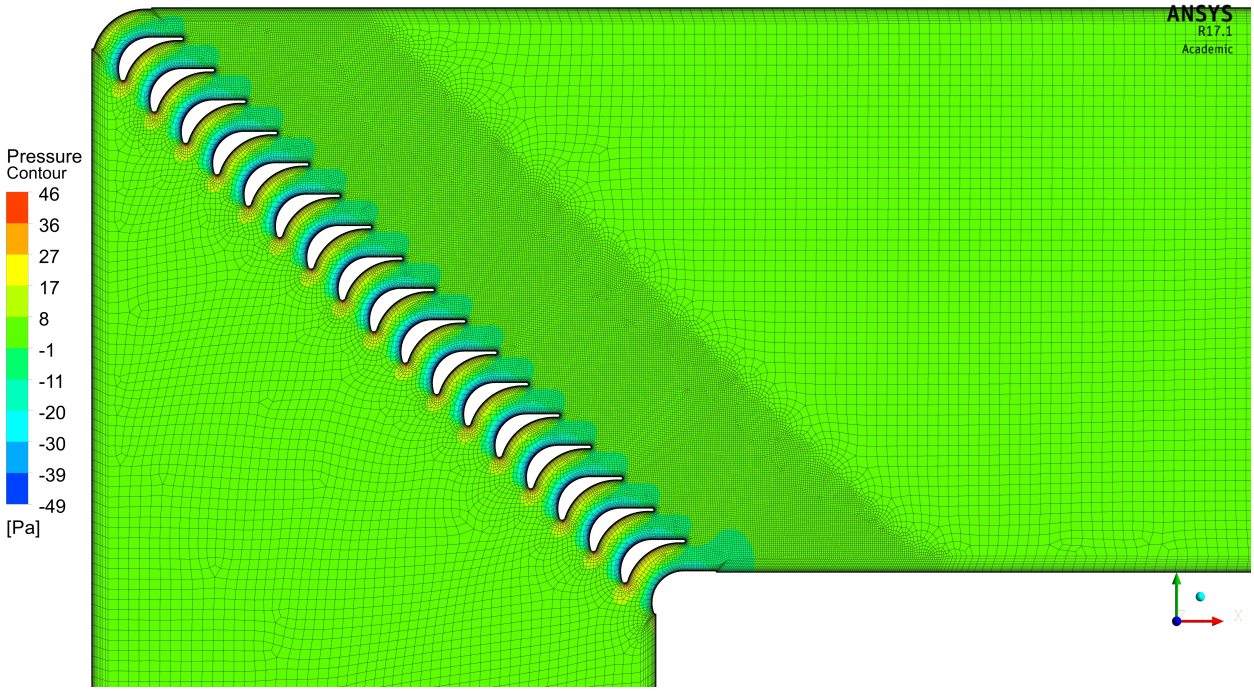

Figure 16. Pressure contour plot for corners three and four. Notice the higher-pressure regions near the bottom of the vanes and the lower pressure at the top of the vanes, which is the expected result for air flow over an airfoil.

Chapter 5

CONCLUSIONS

The purpose of this project was to determine the optimal number of turning vanes for each corner of the Houghton wind tunnel. It was determined which designs minimized the loss of energy through each corner: corners one and two will have 13 vanes and corners three and four will have 19 vanes. The optimal horizontal gap-to-chord ratio of corners 1 and 2 is 0.451 and it is 0.416 for corners 3 and 4. Both are within the range of optimal gaps presented by Klein et al. [21]. The optimal loss coefficients for corners 1 and 2 and corners 3 and 4 based on the simulation data are 0.158 and 0.182, respectively. Both are slightly better than the loss coefficients calculated from the empirical correlations for the preliminary design of the wind tunnel. When compared to experimental data, the present results are lower than loss coefficients reported by Klein et al. [21] and higher than those reported by Collar [20]. The reasons for discrepancies are not clear. However, it should be noted that the double-wall turning vanes tested here are not exactly the same as those used in the experiments, and the present simulation results are not perfectly grid independent.

These optimal designs will be constructed in the next phase of the project so that they can be used and the wind tunnel will be closer to being fully operational. Next, each corner will be built using plywood and acrylic, and the turning vanes will be cut down to size in order to go across the corners. The vanes will be directly mounted to and held in place by 1/8" acrylic on both ends and secured by using 1.5” long 4D finishing nails to fill the holes on

each end. See Figure 17 and Figure 11 to see where the holes are in the vanes. Slots will then be cut out of the corners so that the mounted cascade of vanes can be pulled in and out with little effort if repairs need to be made. Additionally, if a mistake is made in mounting the turning vanes, only a small piece of acrylic needs to be remade and not the entire corner. The vanes will also be smoothed out using Bondo and sanded to smooth ridges of the lock-seam and holes shown in Figure 11. This work will closely accompany the current work that is being done to build the main body of the wind tunnel, and the finalizing and building of the nozzle leading to the test section of the wind tunnel.

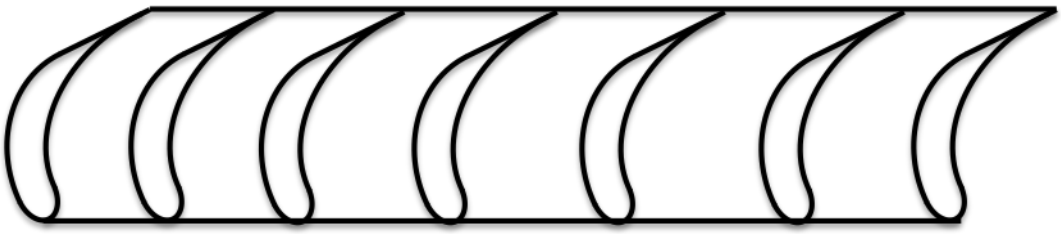

Figure 17. An example of the vane arrays in the corners. 0.125 inch acrylic will be nailed on each side of the vanes to hold it together. It will be slid into grooves in the corner to cap it and redirect the flow.

In the more distant future, pitot-static tubes and data acquisition systems will be added to the wind tunnel construction as well as a balance for the model so that it can be mounted and the aerodynamic forces on it can be observed. The pitot-static tubes will be added to measure the test section speed, and the data acquisition system will be developed to record pressure measurements. Hot wires may also be added to the system to measure velocities. Once the wind tunnel construction is complete, it will be used for various experimental studies including but not limited to fluid dynamics class projects and collaborative projects with businesses outside of Houghton College. This will provide a useful opportunity for undergraduate students to work with a fully operational wind tunnel and will give the

students valuable experience with experimental fluid dynamics. An example of a future project that could be completed is studying the aerodynamic effects of ice accretion on wings. Three-dimensional scans of iced wings can be obtained from researchers at NASA Glenn Research Center. These scans could then be 3D printed and studied using the wind tunnel. The wind tunnel can also be used for projects that specific students are interested in, for example testing new designs for golf balls.

R e f e r e n c e s

[1] D. D. Baals and W. R. Corliss, **Wind Tunnels of NASA** (U.S. Government Printing Office, Washington, D.C., 1981) pp. 1, 9-10.
[2] O. Lilienthal, **Birdflight as the Basis of Aviation** (Longmans, Green, and Co., 1911).
[3] O. Chanute, in **The Aeronautical Annual**, edited by J. Means (W. B. Clarke & Co., Boston, 1897), Vol. 3, Chap. 11, pp. 98-127.
[4] J. B. Barlow, W. H. Rae, Jr., and A. Pope, *Low-Speed Wind Tunnel Testing*, 3rd ed. (John Wiley & Sons, Danvers, MA, 1999).
[5] G. Wickern and N. Lindener, Society of Automotive Engineers, **0868**, 1-19 (2000).
[6] I. Choen, P. Kundu, D. Dowling, **Fluid Mechanics** (Elsevier Science & Technology, 2007).
[7] G. N. Patterson, Aero. Res. Committee Reports and Memoranda No. 1773, 1936 (unpublished).
[8] S. H. Chintamani and R. S. Sawyer, U. S. Patent No. 5,405,106 (11 April 1995).
[9] W. T. Eckert, K. W. Mort, and Jean Pope, NASA TN D-8243 (1976).
[10] A. Sahlin and A. V. Johannson, Physics Fluids A **3**, 1934-1936 (1991).
[11] G. Krober, NACA TM 722, 1932 (unpublished).
[12] Jonathan Jaramillo, B.S. Thesis, Houghton College, 2017.
[13] J. D. Anderson Jr., **Fundamentals of Aerodynamics**, 4th ed. (McGraw-Hill, 2007).
[14] O. Zikanov, **Essential Computational Fluid Dynamics**, 1st ed. (John Wiley & Sons, 2011).
[15] S. C. Speigel, J. R. DeBonis, and H. T. Huynh, Paper No. 1061 presented at 54th AIAA Aerospace Sciences Meeting, San Diego, CA, 2016 (unpublished).
[16] L. J. Clancy, **Aerodynamics** (Halstead Press, New York, 1975).
[17] S. L. Krist, R. T. Beirdon, and C L. Rumsey, NASA TM 208444, 1998.
[18] J. C. Tannehill, D. A. Anderson, and R. H. Pletcher, **Computational Fluid Mechanics and Heat Transfer** (Taylor & Francis, Philadelphia, 1997).
[19] M. Van Dyke, **An Album of Fluid Motion**, (The Parabolic Press, Stanford, CA, 1982).
[20] A. R. Collar, Aero. Res. Committee Reports and Memoranda No.1768, 1937 (unpublished).
[21] G. Klein, K. Tupper, and J. Green, Canadian Journal of Research **3**, 272-285 (1930).